

## Roughness characterization and shearing dislocation failure for rock–backfill interface

Meifeng Cai, Zhilou Feng, Qifeng Guo, Xiong Yin, Minghui Ma, and Xun Xi

Cite this article as:

Meifeng Cai, Zhilou Feng, Qifeng Guo, Xiong Yin, Minghui Ma, and Xun Xi, Roughness characterization and shearing dislocation failure for rock–backfill interface, *Int. J. Miner. Metall. Mater.*, 31(2024), No. 6, pp. 1167-1176. <https://doi.org/10.1007/s12613-024-2901-0>

View the article online at [SpringerLink](#) or [IJMMM Webpage](#).

### Articles you may be interested in

Jia Xiao, Ming Li, Jian-ping Liang, Li Jiang, De-jun Wang, Xiang-xi Ye, Ze-zhong Chen, Na-xiu Wang, and Zhi-jun Li, [Fine structure characterization of an explosively-welded GH3535/316H bimetallic plate interface](#), *Int. J. Miner. Metall. Mater.*, 28(2021), No. 11, pp. 1811-1820. <https://doi.org/10.1007/s12613-020-2128-7>

Sajjad Sattari and Amir Atrian, [Effects of the deep rolling process on the surface roughness and properties of an Al-3vol%SiC nanoparticle nanocomposite fabricated by mechanical milling and hot extrusion](#), *Int. J. Miner. Metall. Mater.*, 24(2017), No. 7, pp. 814-825. <https://doi.org/10.1007/s12613-017-1465-7>

Mohammad A. Omari, Hamzah M. Mousa, Faris M. AL-Oqla, and Mohammad Aljarrah, [Enhancing the surface hardness and roughness of engine blades using the shot peening process](#), *Int. J. Miner. Metall. Mater.*, 26(2019), No. 8, pp. 999-1004. <https://doi.org/10.1007/s12613-019-1818-5>

Yu-ye Tan, Elmo Davide, Yu-cheng Zhou, Wei-dong Song, and Xiang Meng, [Long-term mechanical behavior and characteristics of cemented tailings backfill through impact loading](#), *Int. J. Miner. Metall. Mater.*, 27(2020), No. 2, pp. 140-151. <https://doi.org/10.1007/s12613-019-1878-6>

Qiu-song Chen, Shi-yuan Sun, Yi-kai Liu, Chong-chong Qi, Hui-bo Zhou, and Qin-li Zhang, [Immobilization and leaching characteristics of fluoride from phosphogypsum-based cemented paste backfill](#), *Int. J. Miner. Metall. Mater.*, 28(2021), No. 9, pp. 1440-1452. <https://doi.org/10.1007/s12613-021-2274-6>

Xu Zhao, Andy Fourie, and Chong-chong Qi, [Mechanics and safety issues in tailing-based backfill: A review](#), *Int. J. Miner. Metall. Mater.*, 27(2020), No. 9, pp. 1165-1178. <https://doi.org/10.1007/s12613-020-2004-5>



IJMMM WeChat



QQ author group

# Roughness characterization and shearing dislocation failure for rock–backfill interface

Meifeng Cai<sup>1,2)</sup>, Zhilou Feng<sup>1,2)</sup>, Qifeng Guo<sup>1,2)</sup>,, Xiong Yin<sup>1,2)</sup>, Minghui Ma<sup>3)</sup>, and Xun Xi<sup>1,2)</sup>

1) Key Laboratory of High-Efficient Mine and Safety of Metal Mines of Ministry of Education, Beijing 100083, China

2) Key Laboratory of Urban and Underground Space Engineering, University of Science and Technology Beijing, Beijing 100083, China

3) Shandong Gold Group Co, Ltd, Jinan 250102, China

(Received: 10 March 2024; revised: 1 April 2024; accepted: 2 April 2024)

**Abstract:** Shearing dislocation is a common failure type for rock–backfill interfaces because of backfill sedimentation and rock strata movement in backfill mining goaf. This paper designed a test method for rock–backfill shearing dislocation. Using digital image technology and three-dimensional (3D) laser morphology scanning techniques, a set of 3D models with rough joint surfaces was established. Further, the mechanical behavior of rock–backfill shearing dislocation was investigated using a direct shear test. The effects of interface roughness on the shear–displacement curve and failure characteristics of rock–backfill specimens were considered. The 3D fractal dimension, profile line joint roughness coefficient (JRC), profile line two-dimensional fractal dimension, and the surface curvature of the fractures were obtained. The correlation characterization of surface roughness was then analyzed, and the shear strength could be measured and calculated using JRC. The results showed the following: there were three failure threshold value points in rock–backfill shearing dislocation: 30%–50% displacement before the peak, 70%–90% displacement before the peak, and 100% displacement before the peak to post-peak, which could be a sign for rock–backfill shearing dislocation failure. The surface JRC could be used to judge the rock–backfill shearing dislocation failure, including post-peak sliding, uniform variations, and gradient change, corresponding to rock–backfill dislocation failure on the field site. The research reveals the damage mechanism for rock–backfill complexes based on the free joint surface, fills the gap of existing shearing theoretical systems for isomerism complexes, and provides a theoretical basis for the prevention and control of possible disasters in backfill mining.

**Keywords:** rock–backfill; roughness; correlation characterization; shearing dislocation; interface failure

## 1. Introduction

Due to the requirements for green mine construction, the backfill mining method has been widely adopted in underground mines [1–3]. Because the backfill close to the roof is imperfect, the backfill support for the roof in the space area is limited, and its role is mainly to restrict the lateral deformation of surrounding rock and vertical dislocation during the self-sedimentation of backfill or deformation of surrounding rock. Therefore, the shearing properties of the interfaces between surrounding rocks and backfills significantly affect the stability of backfilled mining goaf [4–5].

In the past decades, considerable research has been conducted on backfill mixtures and mechanical properties [6–7]. For instance, Wu *et al.* [8] developed a low-alkalinity activation method to improve the mechanical performance of cemented rockfill. Meanwhile, a strength prediction model considering the material, ultrasonic, and stress properties of cemented waste rock–backfill for recycling gangue was developed by Wu *et al.* [9]. Zhao *et al.* [10] investigated the effects of water content, water type, and temperature on the

rheological behavior of slag–cement and fly ash–cement paste backfill. Wang *et al.* [11] conducted triaxial cyclic loading and unloading tests to study the mechanical properties and microstructure of layered cemented paste backfill and found that a large number of pores existed in the post-filling layer, which was compacted at early cycles. However, the stability of backfill mining goaf is dependent not only on the properties of the backfill but also on the coupling properties of rock–backfill combination structures.

Indeed, many rock projects involve the mechanics of combined rock strata. In this regard, Xie *et al.* [12] analyzed the influence of surface roughness on the mechanical properties of the combination of dam body and dam foundation. Liu *et al.* [13] studied the shearing failures of combined rock and concrete through direct shearing numerical simulations. Yi *et al.* [14–15] investigated the effects of static load strength, cohesive force, fracture toughness ratio, volume ratio, and interface roughness on the mechanical properties of combined models. The coupling mechanical response of dam bodies and dam foundations at an engineering scale also have been investigated [16–17]. Zuo *et al.* [18–19] focused the damage

✉ Corresponding author: Qifeng Guo E-mail: [guoqifeng@ustb.edu.cn](mailto:guoqifeng@ustb.edu.cn)

© University of Science and Technology Beijing 2024

mechanism for the compressive deformation of coal and rock complexes and proposed a nonlinear model for their failure. Meanwhile, Li *et al.* [20–21] studied the failure process of coal and rock complexes and fractal features from the perspective of impact load and revealed the cooperation mechanism of coal and rock complexes under the action of dynamic disturbance. Chen *et al.* [22] analyzed the influence of coal and rock combination ratios on strength, elastic modulus, and strength before the peak and proposed mechanical models and judgment mechanisms for buckling failure of coal and rock complexes. Yang *et al.* [23] conducted compression tests and numerical simulations considering interfaces and revealed the influencing mechanism of interfaces on the destruction and evolutionary process of complexes.

Existing research on different combinations of rock, concrete, and coal, among others, proves that interfaces play a significant role in the failure of such combinations. However, rock interfaces are normally rough, and the effect of interface roughness on rock–backfill shearing failure has rarely been considered. Thus, this paper took a small unit of surrounding rock and backfill shown in Fig. 1 as the research object and designed shear tests for rock–backfill combinations to investigate the influence of rough joint surfaces on shearing dislocation failure between backfill and surrounding rock, thus guiding the design of backfill mining.

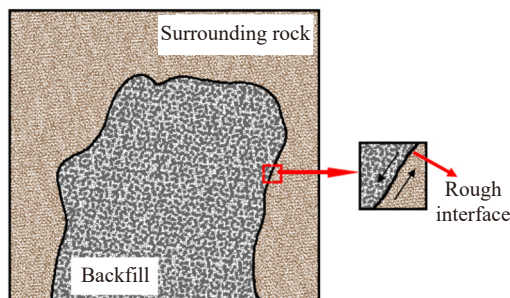


Fig. 1. Diagram for filling in the space area.

## 2. Experimental

Granite is one of the most common rock types in hard-rock mines. To investigate the failure of shearing dislocation between the backfill and surrounding rock based on a free fracture surface, a granite rock beam was broken into a fracture surface with realistic roughness based on the three-point beam bending test and then placed in the mold with the backfill to make a rock–backfill combination for direct shear tests.

### 2.1. Preparation of specimens

After a granite beam of 100 mm × 100 mm × 30 mm was broken through a three-point beam bending test, the surface morphology of the fracture surface was obtained. Then, the granite specimen was placed in a mold, and the backfill was mixed and poured with the granite. The water content of the backfill was 25wt%, and the weight ratio of cement bindings to tailings was 1:3. The rock–backfill combination was demolded after 48 h under an indoor environment and then put

into a standard curing box for 28 d. Fig. 2 shows an example of the final specimen.



Fig. 2. Rock–backfill specimen.

### 2.2. Test methods

A Talysurf CLI2000 three-dimensional (3D) laser morphology scanner was used to conduct the overall scanning and modeling for the fracture surface of the granite. 3D data of the fracture surface were imported as 3D surface cloud pictures into software to quantify surface roughness.

A direct shearing device was used to conduct shear tests for the rock–backfill combination, and a digital image correlation (DIC) device was used to monitor the shearing failure process to study the failure for shearing dislocation between the backfill and the surrounding rock. The rock–backfill shear test was conducted using the rock shearing testing machine (TFD-20H/50J) produced by Changchun Keyi Test Instrument Co., Ltd. The normal peak load was 20 kN, and the tangential peak load was 50 kN. During the shearing process, a displacement control method was used. The shearing rate was 0.1 mm/min. A StrainMaster Portable strain measurement system (DIC devices) produced by LaVision in Germany was used to conduct real-time monitoring for the surface deformation of test specimens and record the shearing deformation process of complex specimens. The test system was arranged as shown in Fig. 3.

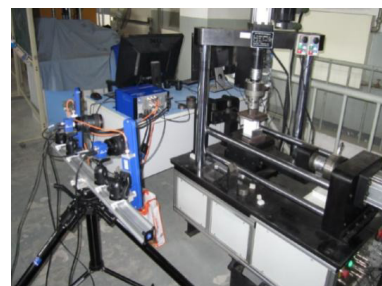


Fig. 3. Photograph of test system.

## 3. Acquisition of roughness parameters for the free fracture surface

JRC is an important parameter that measures the roughness of a joint. It is also one of the important factors that affect the mechanical behavior of rock–backfill specimens. For the rock–backfill combination, the interface between the rock

and the backfill was dependent on the surface of the rock, which could be characterized by JRC. Joint surfaces are generally random and ruleless. Thus, describing roughness through quantification is of great significance. At the earliest, Barton and Choubey [24] put forward a concept for describing the roughness degree of a structural surface with JRC through tests and gave 10 typical roughness joints where JRC ranged from 0 to 20 in 1976. For an unknown curve, we can compare it with the Barton standard curve to get its JRC.

Mandelbrot [25] created fractal geometry theory in 1967, which was first introduced by Turk *et al.* [26] to JRC research in 1987, and the quantitative relation between fractal dimension and JRC was established thereby. Fractal is a collection of similar bodies; the joint hatching line has overall similarity, and the up-and-down details are of statistical significance and meet the definition of fractal. Therefore, the fractal theory's advantages of being used for joint roughness are congenital.

Ten Barton standard curves put forward by Barton did not give a definite JRC value. The relational expression of JRC and fractal dimension established by Xie [27] is one of the methods that are widely used to calculate JRC based on fractal dimension at present.

This paper chose the box fractal dimension method to measure the fractal dimension value of different Barton curves and completed the quantification of JRC based on Eq. (1).

$$JRC = 85.2671(D - 1)^{0.5679} \quad (1)$$

where  $D$  represents fractal dimension.

The box fractal dimension method [28] uses grids with a side length of  $\delta$  to cover the figure that must be measured and calculates the number of boxes required to cover the whole figure. The side length of boxes must be continuously reduced to obtain the number of boxes required to cover the figure under different side lengths. Using the equation for box fractal dimension, the special box fractal dimension is obtained, and two-dimensional boxes are changed to three-dimensional cubes. The method can be mapped to three-dimensional figures.

### 3.1. Steps for extracting information for fracture bodies

After the granite rock beam was broken through the three-point bending test, a 3D laser morphology scanner was used to conduct overall scanning for the fracture bodies of the granite to obtain a 3D cloud picture. Only the 3D fracture bodies near the fracture surface were related to the roughness

of the fracture surface. Therefore, a 3D surface cloud picture was used to characterize the surface roughness. The specific process is as follows:

(1) Define the coordinates of the 3D surface cloud picture again and generate a new entity coordinate system.

(2) Convert the 3D surface cloud picture into a 3D entity to facilitate subsequent section and operation. The digital scanning surface cloud picture before conversion is shown in Fig. 4(a), and the entity picture after conversion is shown in Fig. 4(b).

(3) Position the wave crest and trough of the fracture surface through a section and cut off the area outside the zone of fracture according to the coordinates of the crest and trough to generate the new entity of the zone of fracture, as shown in Fig. 4(c).

(4) Complete the section, calculation of fractal dimension, curvature, and other parameters, data export, and other subsequent operations on the new entity of the zone of fracture.

### 3.2. Method of calculating roughness parameters of fracture bodies

The roughness parameters of fracture bodies include the three-dimensional fractal dimension, two-dimensional profile fractal dimension, JRC, and surface curvature of the fracture surface. The method of calculating them is as follows:

(1) Three-dimensional fractal dimension.

Based on an unfixed boundary, this is calculated using the box fractal dimension method shown in Eq. (2):

$$D_B = -\lim_{\delta \rightarrow 0} \frac{\ln N_\delta(F)}{\ln \delta} = \lim_{\delta \rightarrow 0} \frac{\ln N_\delta(F)}{\ln(1/\delta)} \quad (2)$$

where  $D_B$  refers to the box fractal dimension,  $\delta$  refers to the side length of the grid cover mass,  $F$  refers to the fractal set, and  $N_\delta(F)$  refers to the number of boxes.

(2) Two-dimensional profile fractal dimension.

Using the box fractal dimension method shown in Eq. (2), the specimen was divided into a two-dimensional section to calculate the box fractal dimension of a two-dimensional profile and the mean value. The typical profile during the computational process is shown in Fig. 5.

(3) JRC.

To calculate JRC according to the two-dimensional profile fractal dimension, take specimen 1-1 as the object and select 20 profiles with equal spacing. First, demarcate the JRC of 20 profiles according to the Barton standard curve. Then, calculate the two-dimensional fractal dimension of all profiles. Afterward, based on Eq. (1) fitting, obtain the relation-

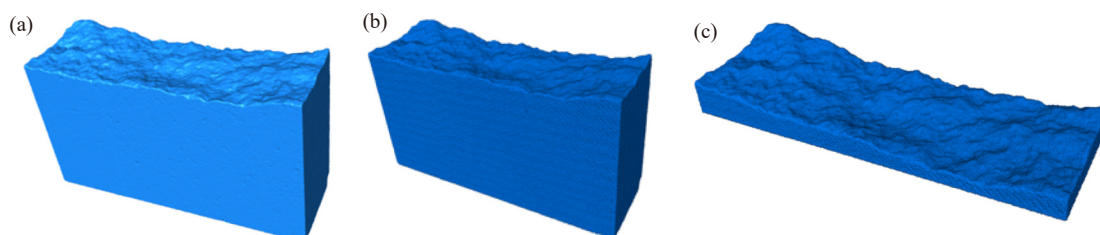


Fig. 4. Process for extracting fracture bodies: (a) digital scanning surface cloud picture; (b) volume rendering entity picture; (c) zone of fracture.



**Fig. 5. Typical profile maps in calculating the profile fractal dimension: (a) map 1; (b) map 2; (c) map 3.**

ship between the fractal dimension of specimen 1-1 and JRC, as shown in Eq. (3). Lastly, calculate the JRC of all profiles according to Eq. (3) and the mean value.

$$\text{JRC} = 21.07(D - 1)^{0.49} \quad (3)$$

(4) Surface curvature.

The Generate Surface command was used to generate a surface cloud picture of fracture bodies. The Curvature and Surface View commands were used to view the surface curvature of the fracture surface, whereas the Histogram command was used to view the value of the surface curvature.

### 3.3. Calculation result

The result of calculating the 3D fractal dimension of fracture bodies, profile line JRC mean value, profile line two-dimensional fractal dimension mean value, and surface curvature of the fracture surface with the above methods are shown in Table 1. The 3D fractal dimension of fracture bodies, profile line JRC mean value, and profile line two-dimensional fractal dimension mean value had a good consistency. The JRC of fracture bodies ranged from 12 to 18, consistent with those calculated using the Barton standard curve during a preliminary study [29]. The surface curvature of the fracture surface was weak compared with other parameters.

The surface curvature plot of the fracture surface generated by 16 specimens and the fracture surface under volume rendering are shown in Fig. 6. The middle-upper part of each specimen drawing belonged to the fracture surface of rendering, whereas the lower part was the surface curvature plot of the fracture surface. The colors show the differences in the surface curvature. The closer the color to red, the larger the surface curvature.

Fig. 6 shows that JRC matched the surface curvature relatively. Taking specimens 1-1, 1-2, 2-1, and 2-2 as examples, specimen 1-2 had a wide red area and large quantity, corresponding to the maximum JRC; meanwhile, specimen 2-1 had a narrow red area and small quantity, corresponding to the minimum JRC. However, as far as some specimens were concerned, the surface curvature was not consistent with JRC, indicating that measuring the applicability of JRC with surface curvature had limitations to a certain extent.

## 4. Free fracture surface fractal dimension and roughness correlation characterization

### 4.1. JRC and profile fractal dimension

Fig. 7 shows the relationship between JRC and the mean fractal dimension of a profile. Both had extremely good index-fitting relationships, as shown in Eq. (4). The coefficient of determination is 0.999.

$$\text{JRC} = 43.278 \times D^{0.434} - 36.688 \quad (4)$$

The fitting equation provides new thought for JRC calculation. JRC can be calculated directly after the two-dimensional fractal dimension mean value is obtained, which is a more convenient way for calculating the mean value compared with Eq. (3) requiring JRC calculation first.

### 4.2. Fractal dimension of fracture bodies and profile

Fig. 8 shows the relationship between the fractal dimen-

**Table 1. JRC of the free fracture surface, fractal dimension, and surface curvature**

No.	3D fractal dimension of fracture bodies	Profile line JRC mean value	Profile line two-dimensional fractal dimension mean value	Surface curvature of the fracture surface
1-1	2.564	15.862	1.564	2.001
1-2	2.528	16.466	1.609	1.961
2-1	2.400	13.826	1.426	1.960
2-2	2.560	15.548	1.543	2.064
3-1	2.354	13.229	1.389	1.151
3-2	2.560	16.414	1.603	2.046
4-1	2.441	15.816	1.559	2.401
4-2	2.495	15.234	1.523	2.030
5-1	2.432	15.053	1.507	2.641
5-2	2.427	14.957	1.504	2.248
6-1	2.495	14.621	1.483	2.117
6-2	2.332	13.719	1.420	0.721
7-1	2.498	16.070	1.577	1.699
7-2	2.491	14.878	1.497	2.199
8-1	2.511	14.984	1.507	1.587
8-2	2.319	12.835	1.367	1.191

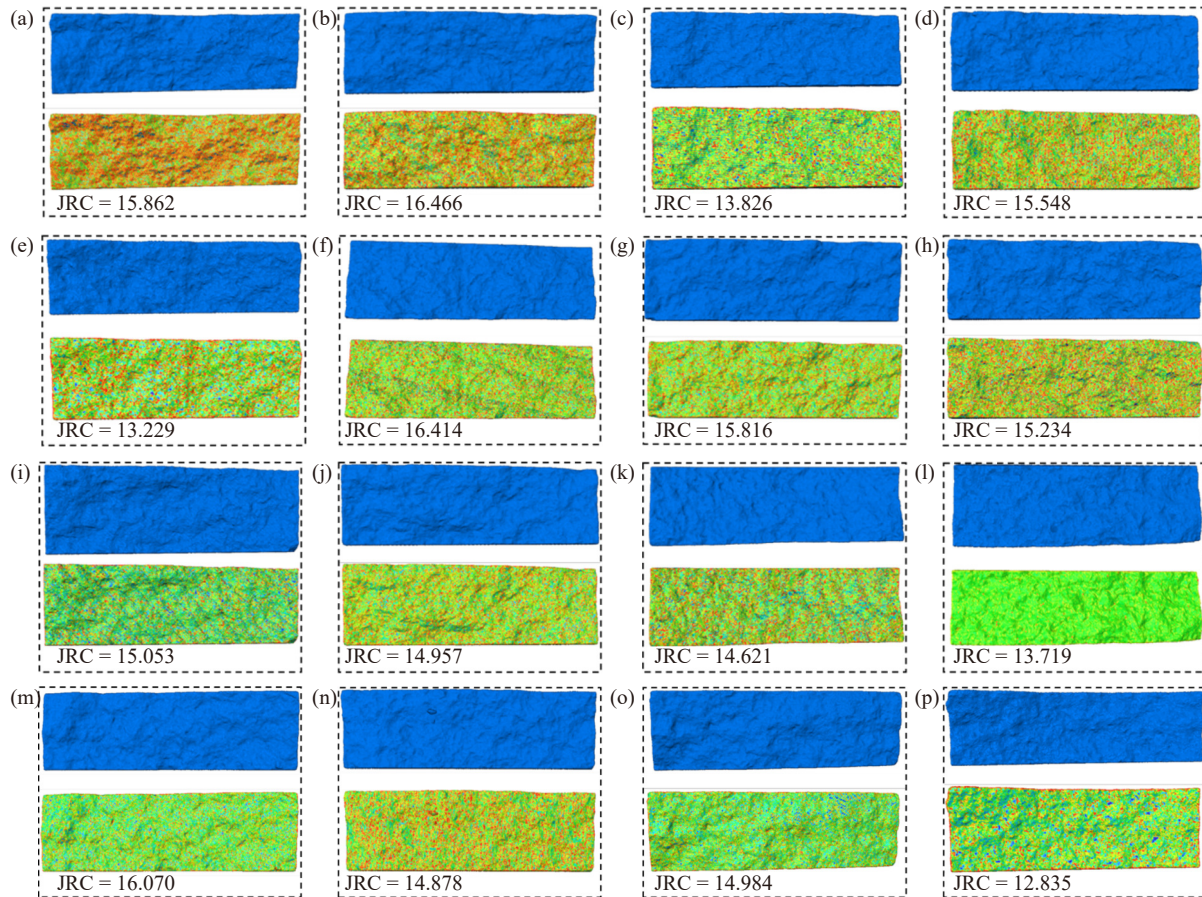


Fig. 6. Surface curvature of the fracture surface: (a) specimen 1-1; (b) specimen 1-2; (c) specimen 2-1; (d) specimen 2-2; (e) specimen 3-1; (f) specimen 3-2; (g) specimen 4-1; (h) specimen 4-2; (i) specimen 5-1; (j) specimen 5-2; (k) specimen 6-1; (l) specimen 6-2; (m) specimen 7-1; (n) specimen 7-2; (o) specimen 8-1; (p) specimen 8-2.

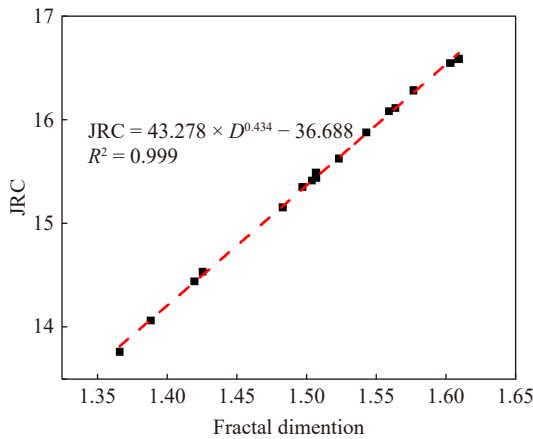


Fig. 7. Relationship between JRC and the mean fractal dimension of a profile.

sion of fracture bodies and the mean fractal dimension of the profile. Both had good linear growth relationships. The linear fitting relationship is shown in Eq. (5).

$$y = 0.941x + 1.046 \tag{5}$$

### 4.3. JRC and fractal dimension of fracture bodies

Fig. 9 shows the relationship between JRC and the fractal dimension of fracture bodies. Both had good linear correlations as well. The linear fitting relationship is shown in Eq.

(6), and the coefficient of determination is 0.736. The correlation between two-dimensional JRC was obtained according to the three-dimensional fractal dimension and profile line, and the three-dimensional fractal dimension could characterize the roughness of fracture bodies.

$$JRC = 11.757 \times D - 13.988 \tag{6}$$

### 4.4. JRC and shear strength

Fig. 10 shows the relationship between shear strength  $\tau$  and JRC. Both had quadratic function relationships, as shown in Eq. (7). The coefficient of determination is 0.968.

$$\tau = -0.002713JRC^2 + 0.227637JRC - 1.49246 \tag{7}$$

where  $\tau$  is the shear strength.

Substituting Eq. (6) into Eq. (7), we can predict the shear strength with fracture dimension, and the expression is as follows:

$$\tau = -0.002713 \times (11.757D - 13.988)^2 + 0.227637 \times (11.757D - 13.988) - 1.49246 \tag{8}$$

With the value of the three-dimensional fracture dimension, we can obtain the calculated shear strength and actual shear strength using Eq. (8), as shown in Fig. 11. The error mean of both is 4.99%, indicating that Eq. (8) is relatively reliable and the shear strength and three-dimensional fracture dimension have a quadratic function relationship. With the

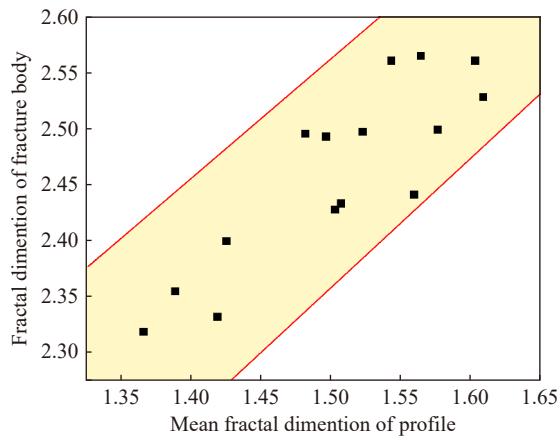


**Fig. 8.** Relationship between the fractal dimension of fracture bodies and the mean fractal dimension of a profile.

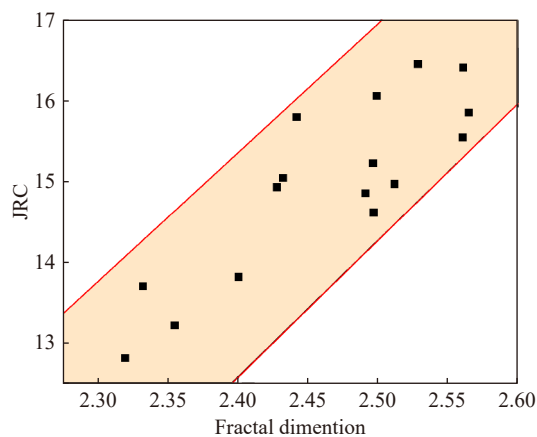


**Fig. 9.** Relationship between JRC and the fractal dimension of fracture bodies.

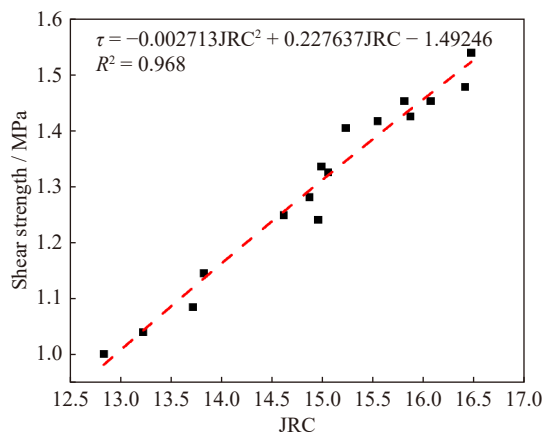


**Fig. 10.** Relationship between shear strength and JRC.

increase in the three-dimensional fracture dimension, the shear strength also continues increasing, and the fundamental reason lies in the increase in the roughness.

## 5. Rock–backfill shearing dislocation failure

### 5.1. Rock–backfill shear stress–displacement

Fig. 12 shows the rock–backfill shear stress–displacement curve of different specimens. JRC was from low to high. The

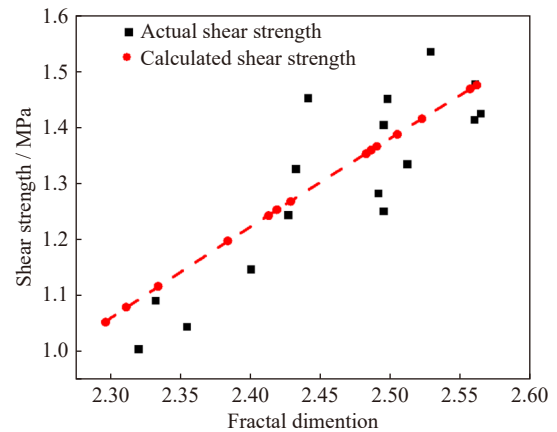


**Fig. 11.** Relationship between calculated shear strength and actual shear strength.

shear stress–displacement curve entered a slip stage, uniform descent section, and stepwise descent section after a peak shear stress point was achieved. The JRC threshold values of the three curves were 12–14, 14–16, and 16–18, respectively. The different curve types mainly depended on the proportion of steep joint peaks and gentle joint peaks on the rough surface. The wear conditions of the interface from the backfill side were more significant than those from the rock side because the backfill was much weaker than the rock. Therefore, the rough joint was a key factor that decided the rock–backfill shear stress–displacement curve and JRC parameters that could be used for judging different curve types.

### 5.2. Rock–backfill shearing dislocation failure before the peak

Fig. 13 shows the strain field during typical rock–backfill failure. When there was a 10% displacement before the peak, there was a small range of displacement around the complex because of the boundary effect of the shear stress load. When there was a 30% displacement before the peak, the joint profile was shown on the strain cloud picture. When there was a 50% displacement before the peak, the shape change of the joint surface increased, and the peak strain value increased by 250% compared with that when there was a 30% displacement before the peak. When there was a 70% displacement before the peak, the complex profile had a shape change under the action of shear force. When there was a 90% displacement before the peak, the joint surface of the complex was damaged, and the joint surface slipped, resulting in the failure of the partial joint peak. When there was a 100% displacement before the peak, the partial joint peak had a brittle failure, and the joint surface could not be engaged. The strain cloud picture also had fault phenomena.

### 5.3. Shearing dislocation failure of rock–backfill after the peak

Fig. 14 shows a simplified rock–backfill model. A small microbody in the interface of the backfill and granite was taken to conduct an analysis. During the shear test, there was fixed axial stress above, below, and on two sides of the complex to ensure that the shear test could be conducted nor-

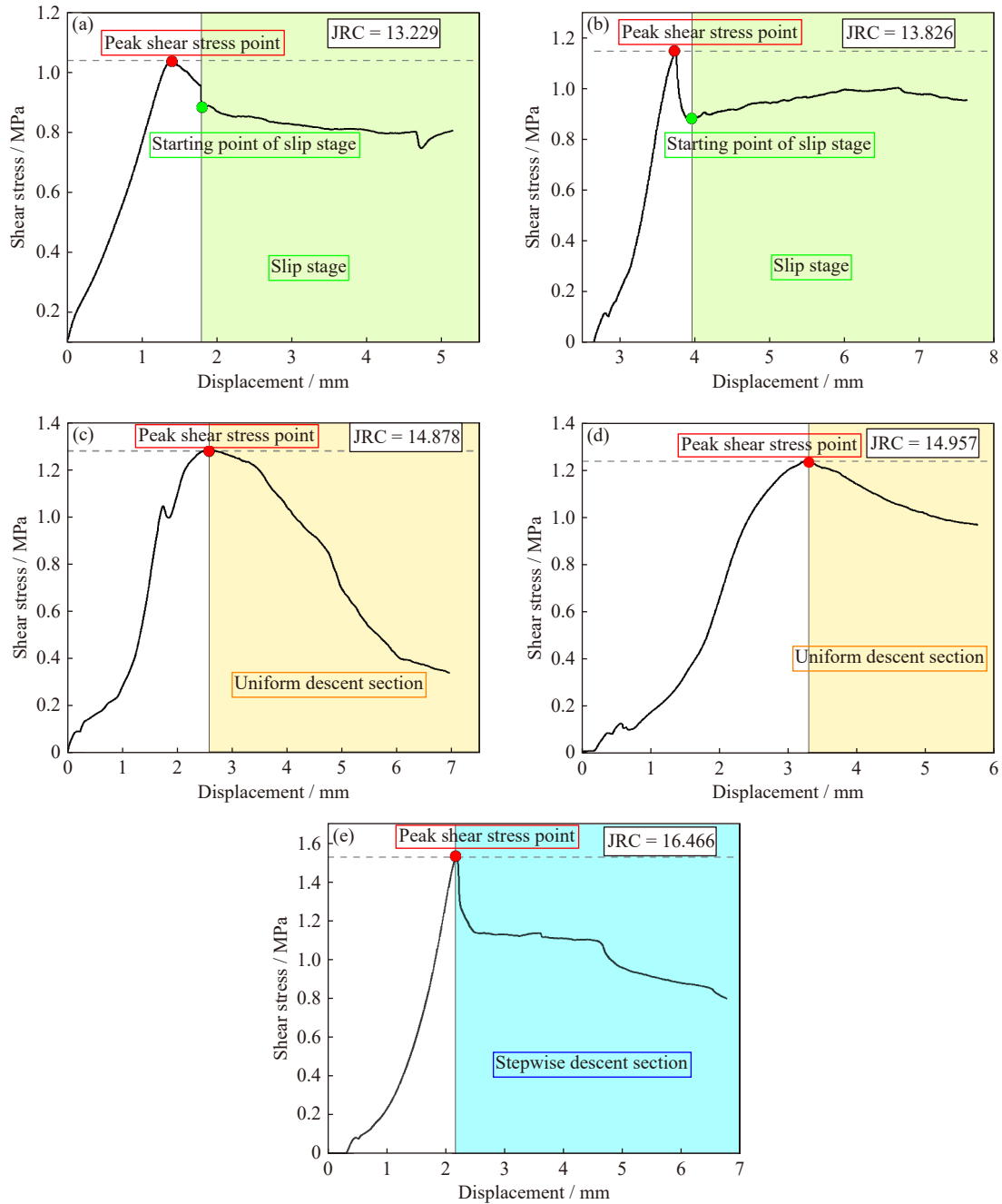


Fig. 12. Rock–backfill shear stress–displacement curve: (a) specimen 3-1; (b) specimen 2-1; (c) specimen 7-2; (d) specimen 5-2; (e) specimen 1-2.

mally. The stress refers to  $\sigma_2$  in the figure. The test system exerted shear force on the complex from right to left, and force was directly exerted on the backfill, forming  $\sigma_{1B}$ . At this time, because of the counteracting force of the fixed bin, the granite also underwent  $\sigma_{1G}$  rightward. Because the elasticity modulus of granite was larger than that of the backfill, the backfill produced external expansion failure before granite after being impacted by an external force. However, because of the cohesive force, the bonding surface exerted an inward restraining force, that is,  $\sigma_{3B}$ , and it exerted a counteracting force  $\sigma_{3G}$  on the granite at the same time. At this time, the backfill component was under compressive stress in three directions, whereas the granite was under a pulling-com-

pressive stress state. According to the Griffith theory [30], the strength of the granite component close to the bonding surface is weaker than that of the granite in other parts and the strength of the backfill component is larger than the backfill in other parts.

With the boundary of the contact surface, the complex was divided into four parts: granite close to the bonding surface, granite away from the bonding surface, backfill close to the bonding surface, and backfill away from the bonding surface. For the granite, the strength of the granite away from the bonding surface was larger than that of the granite close to the bonding surface. For the backfill, the strength of the backfill close to the bonding surface was larger than that of

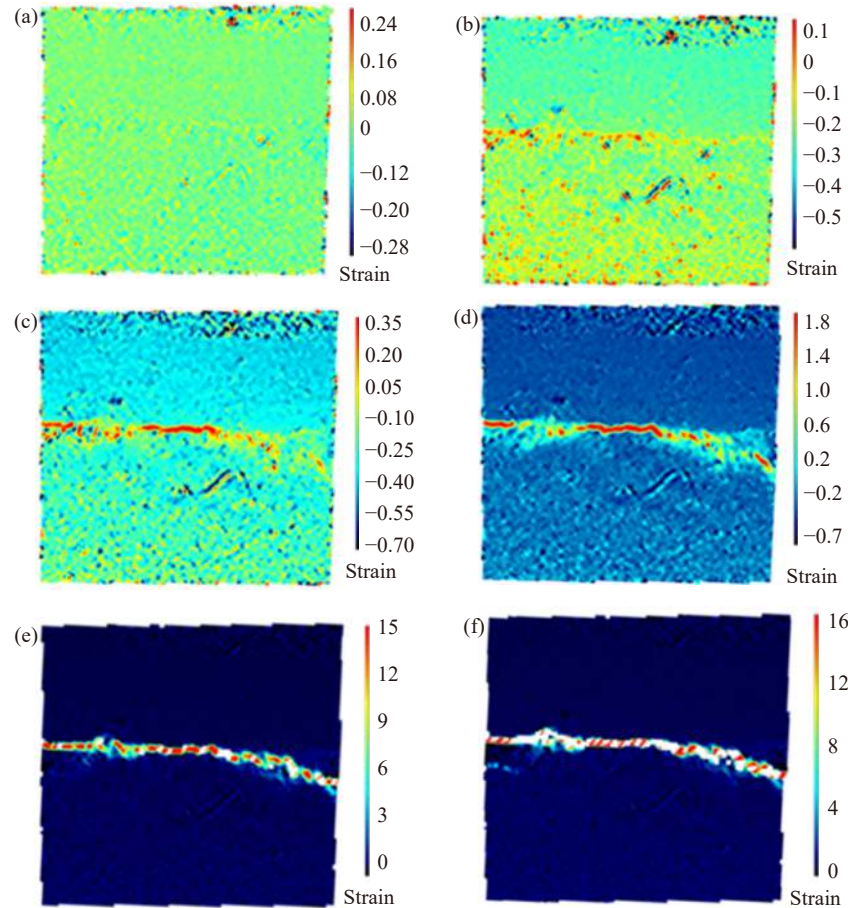


Fig. 13. Rock–backfill failure at different displacements before the peak: (a) 10%; (b) 30%; (c) 50%; (d) 70%; (e) 90%; (f) 100%.

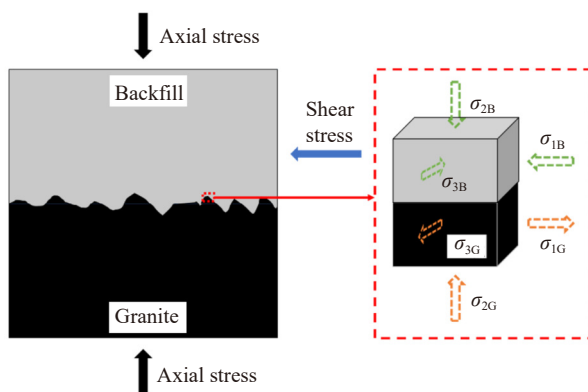


Fig. 14. Simplified rock–backfill model.

the backfill away from the bonding surface. Typical rock–backfill DIC strain cloud pictures after the peak based on the free fracture surface of 16 specimens were selected, as shown in Fig. 15.

After the peak, the granite close to the bonding surface showed obvious shape change and damage. The reason was that the fracture surface had many secondary microcracks after the granite was crushed through the bending test under three-point loading, resulting in low strength in the component of the granite close to the bonding surface. After being impacted by shear stress, the steep joint peak was stressed, which awakened the secondary cracks nearby, extended the connection, and produced the main defect surface until brittle

failure.

During actual engineering, after the surrounding rock in the stope undergoes external loading, such as drilling and blasting, the main defect surface causes the surrounding rock to fall and break and produces many secondary cracks near the defect surface. After the slurry is filled, the secondary cracks of the surrounding rock near the bonding surface still exist. Because of the acting force of the bonding surface and secondary cracks, the surrounding rock more easily undergoes brittle failure, resulting in potential hazards.

## 6. Conclusions

The paper designed a rock–backfill shearing dislocation test method in combination with digital image technology and 3D laser morphology scanning technology. A set of 3D modeling processes with rough joint surfaces was established, and the mechanical behavior and failure of rock–backfill shearing dislocation based on the free joint surface were investigated. The main conclusions were drawn as follows:

(1) The developed method of the rough joint surface in this paper can be used to obtain the 3D fractal dimension of a rough surface, profile line two-dimensional fractal dimension mean values, and the surface curvature of the fracture surface. The correlation characterization of surface roughness can be realized through correlation analysis.

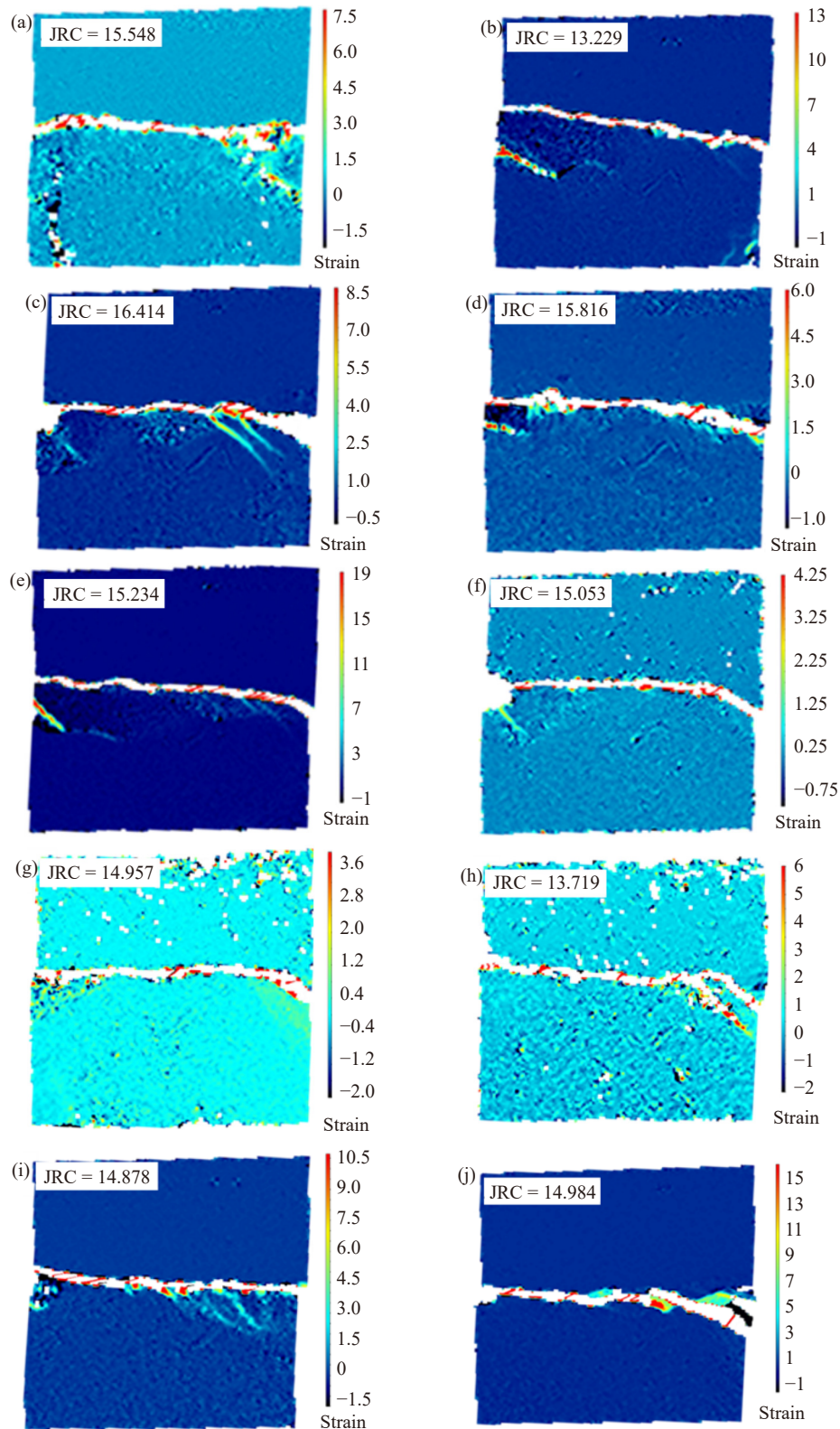


Fig. 15. Rock–backfill failure after the peak of different specimen: (a) specimen 2-2; (b) specimen 3-1; (c) specimen 3-2; (d) specimen 4-1; (e) specimen 4-2; (f) specimen 5-1; (g) specimen 5-2; (h) specimen 6-2; (i) specimen 7-2; (j) specimen 8-1.

(2) The 3D fractal dimension of fracture bodies and profile line two-dimensional fractal dimension mean value had a good consistency. The relationship between the shear strength of the interface and the fractal dimensions was established.

(3) The rock–backfill complex had three failure threshold

value points in total, located in 30%–50% displacement before the peak, 70%–90% displacement before the peak, and 100% displacement before the peak to post-peak, respectively. The shear stress–displacement curve of the complex could be classified into three categories: slip, uniform descent, and stepwise descent after the peak.

The shear dislocation of the rock–backfill interface was also affected by normal stress, which was not considered in the present work. Thus, the developed model for predicting interface shear dislocation needs to be improved by considering normal stress in future works.

## Acknowledgements

This work is supported by the National Key Research and Development Program of China (No. 2021YFC3001302) and the National Natural Science Foundation of China (No. 52274072).

## Conflict of Interest

Meifeng Cai is an advisory board member for this journal and was not involved in the editorial review or the decision to publish this article. The authors declare that they have no known competing financial interests or personal relationships that could have appeared to influence the work reported in this paper.

## References

- [1] X. Zhao, A. Fourie, and C.C. Qi, Mechanics and safety issues in tailing-based backfill: A review, *Int. J. Miner. Metall. Mater.*, 27(2020), No. 9, p. 1165.
- [2] M. Wang, X. Xi, Q.F. Guo, J.L. Pan, M.F. Cai, and S.T. Yang, Sulfate diffusion in coal pillar: Experimental data and prediction model, *Int. J. Coal Sci. Technol.*, 10(2023), No. 1, p. 12.
- [3] Q.F. Guo, X. Xi, S.T. Yang, and M.F. Cai, Technology strategies to achieve carbon peak and carbon neutrality for China's metal mines, *Int. J. Miner. Metall. Mater.*, 29(2022), No. 4, p. 626.
- [4] P.T. Wang, Z.J. Huan, F.H. Ren, L. Zhang, and M.F. Cai, Research on direct shear behaviour and fracture patterns of 3D-printed complex jointed rock models, *Rock Soil Mech.*, 41(2020), art. No. 46.
- [5] Y.Y. Tan, X. Yu, D. Elmo, L.H. Xu, and W.D. Song, Experimental study on dynamic mechanical property of cemented tailings backfill under SHPB impact loading, *Int. J. Miner. Metall. Mater.*, 26(2019), No. 4, p. 404.
- [6] Y.Y. Tan, E. Davide, Y.C. Zhou, W.D. Song, and X. Meng, Long-term mechanical behavior and characteristics of cemented tailings backfill through impact loading, *Int. J. Miner. Metall. Mater.*, 27(2020), No. 2, p. 140.
- [7] H.Y. Cheng, S.C. Wu, X.Q. Zhang, and A.X. Wu, Effect of particle gradation characteristics on yield stress of cemented paste backfill, *Int. J. Miner. Metall. Mater.*, 27(2020), No. 1, p. 10.
- [8] J.Y. Wu, H.S. Wong, H. Zhang, Q. Yin, H.W. Jing, and D. Ma, Improvement of cemented rockfill by premixing low-alkalinity activator and fly ash for recycling gangue and partially replacing cement, *Cem. Concr. Compos.*, 145(2024), art. No. 105345.
- [9] J.Y. Wu, H.W. Jing, Q. Yin, L.Y. Yu, B. Meng, and S.C. Li, Strength prediction model considering material, ultrasonic and stress of cemented waste rock backfill for recycling gangue, *J. Clean. Prod.*, 276(2020), art. No. 123189.
- [10] Y. Zhao, A. Taheri, M. Karakus, Z.W. Chen, and A. Deng, Effects of water content, water type and temperature on the rheological behaviour of slag-cement and fly ash-cement paste backfill, *Int. J. Min. Sci. Technol.*, 30(2020), No. 3, p. 271.
- [11] J. Wang, J.X. Fu, and W.D. Song, Mechanical properties and microstructure of layered cemented paste backfill under triaxial cyclic loading and unloading, *Constr. Build. Mater.*, 257(2020), art. No. 119540.
- [12] H.P. Xie, Z.H. Chen, H.W. Zhou, C. Yi, and Z.J. Chen, Study on two-body mechanical model based on interaction between structural body and geo-body, *Chin. J. Rock Mech. Eng.*, 24(2005), No. 9, p. 1457.
- [13] X.R. Liu, H.W. Zhou, and H. Li, Numerical simulation of interface behavior in rock-concrete interaction problem, *Chin. J. Rock Mech. Eng.*, 24(2005), No. S2, p. 5648.
- [14] C. Yi, H.G. Zhu, H.T. Wang, Z. Liu, and H. Pan, Analysis of transformation conditions and influence factors of uni-body and bi-body models under axial compression, *Rock Soil Mech.*, 32(2011), No. 5, p. 1297.
- [15] C. Yi, L. Zhang, Z.H. Chen, and H.P. Xie, Experimental study on bi-material and bi-body models under axial compression, *Rock Soil Mech.*, 27(2006), No. 4, p. 571.
- [16] K. Mandal and D. Maity, Transient response of concrete gravity dam considering dam-reservoir-foundation interaction, *J. Earthq. Eng.*, 22(2018), p. 211.
- [17] Y. Chen, L. Zhang, B.Q. Yang, J.H. Dong, and J.Y. Chen, Geomechanical model test on dam stability and application to Jinping High arch dam, *Int. J. Rock Mech. Min. Sci.*, 76(2015), p. 1.
- [18] J.P. Zuo, Y. Chen, and H.Q. Song, Study progress of failure behaviors and nonlinear model of deep coal-rock combined body, *J. Cent. South Uni. Sci. Technol.*, 52(2021), No. 8, p. 2510.
- [19] J.P. Zuo, J.L. Pei, J.F. Liu, R.D. Peng, and Y.C. Li, Investigation on acoustic emission behavior and its time-space evolution mechanism in failure process of coal–rock combined body, *Chin. J. Rock Mech. Eng.*, 30(2011), No. 8, p. 1564.
- [20] C.J. Li, Y. Xu, and Z.Y. Ye, Energy dissipation and crushing characteristics of coal–rock-like combined body under impact loading, *Chin. J. Geotechn. Eng.*, 42(2020), No. 5, p. 981.
- [21] C.J. Li, Y. Xu, Y.T. Zhang, and H.L. Li, Study on energy evolution and fractal characteristics of cracked coal–rock-like combined body under impact loading, *Chin. J. Rock Mech. Eng.*, 38(2019), No. 11, p. 2231.
- [22] G.B. Chen, T. Li, L. Yang, G.H. Zhang, J.W. Li, and H.J. Dong, Mechanical properties and failure mechanism of combined bodies with different coal–rock ratios and combinations, *J. Min. Strata Control Eng.*, 3(2021), No. 02, p. 84.
- [23] K. Yang, W.J. Liu, L.T. Dou, X.L. Chi, Z. Wei, and Q. Fu, Experimental investigation into interface effect and progressive instability of coal–rock combined specimen, *J. China Coal Soc.*, 45(2020), No. 5, p. 1691.
- [24] N. Barton and V. Choubey, The shear strength of rock joints in theory and practice, *Rock Mech.*, 10(1977), No. 1, p. 1.
- [25] B. Mandelbrot, How long is the coast of Britain? Statistical self-similarity and fractional dimension, *Science*, 156(1967), No. 3775, p. 636.
- [26] N. Turk, M.J. Greig, W.R. Dearman, and F. Amin, Characterization of rock joint surfaces by fractal dimension, [in] *The 28th US Symposium on Rock Mechanics (USRMS)*, OnePetro, 1987.
- [27] H.P. Xie, Fractal description of rock joints, *Chin. J. Geotech. Eng.*, 17(1995), No. 1, p. 18.
- [28] M.H. Ma, *Collaborative Bearing Mechanism of Surrounding Rock–backfill and Stability Analysis in Residual Ore Recovery* [Dissertation], University of Science and Technology Beijing, Beijing, 2023.
- [29] S.B. Chen, X.W. Pan, and J.F. Liu, Impact localization method based on the partial least squares regression fractal dimension, *J. Vibr. Shock*, 40(2021), No. 2, p. 97.
- [30] W.F. Brace, An extension of the Griffith theory of fracture to rocks, *J. Geophys. Res.*, 65(1960), No. 10, p. 3477.